Boundary-Layer Meteorol (2013) 147:139–163
DOI 10.1007/s10546-012-9776-8

ARTICLE

Air–Sea Interaction Features in the Baltic Sea and at a Pacific Trade-Wind Site: An Inter-comparison Study

Ulf Högström · Anna Rutgersson · Erik Sahlée · Ann-Sofi Smedman · Tihomir S. Hristov · W. M. Drennan · K. K. Kahma

Received: 4 April 2012 / Accepted: 16 October 2012 / Published online: 3 November 2012

Abstract A systematic comparison of wind profiles and momentum exchange at a trade wind site outside Oahu, Hawaii and corresponding data from the Baltic Sea is presented. The trade wind data are to a very high degree swell dominated, whereas the Baltic Sea data include a more varied assortment of wave conditions, ranging from a pure growing sea to swell. In the trade wind region swell waves travel predominantly in the wind direction, while in the Baltic, significant cross-wind swells are also present. Showing the drag coefficient as a function of the 10-m wind speed demonstrates striking differences for unstable conditions with swell for the wind-speed range $2\,\mathrm{m\,s^{-1}} < U_{10} < 7\,\mathrm{m\,s^{-1}}$, where the trade-wind site drag values are significantly larger than the corresponding Baltic Sea values. In striking contrast to this disagreement, other features studied are surprisingly similar between the two sites. Thus, exactly as found previously in Baltic Sea studies during unstable conditions and swell, the wind profile in light winds ($3\,\mathrm{m\,s^{-1}}$) shows a wind maximum at around 7–8 m above the water, with close to constant wind speed above. Also, for slightly higher wind speeds ($4\,\mathrm{m\,s^{-1}} < U_{10} < 7\,\mathrm{m\,s^{-1}}$), the similarity between wind profiles is striking, with a strong wind-speed increase below a height of about 7–8 m followed by a layer of virtually constant wind speed above. A consequence of these wind-profile features is that Monin–Obukhov similarity is no longer valid. At the trade-wind site this was observed to be the case even for wind speeds as high as $10\,\mathrm{m\,s^{-1}}$. The turbulence kinetic energy budget was evaluated for

U. Högström (✉) · A. Rutgersson · E. Sahlée · A.-S. Smedman
Department of Earth Sciences, Meteorology, University of Uppsala, 75236 Uppsala, Sweden
e-mail: ulf.hogstrom@met.uu.se

T. S. Hristov
Department of Mechanical Engineering, Johns Hopkins University, Baltimore, MD, USA

W. M. Drennan
Rosenstiel School of Marine and Atmospheric Science, University of Miami, Miami, FL 33149-1098, USA

K. K. Kahma
Finnish Meteorological Institute, 00101 Helsinki, Finland

four cases of 8–16 30-min periods at the trade-wind site, giving results that agree very well with corresponding figures from the Baltic Sea.

Keywords Air–sea interaction · Monin–Obukhov similarity · Swell turbulence · Wind profiles

1 Introduction

Parametrizations of air–sea exchange in atmospheric numerical models are often based on the COARE (Coupled Ocean–Atmosphere Response Experiment) model, see e.g. Fairall et al. (2003), or a similar scheme. The COARE model in turn is based on numerous field experiments in various oceanic areas. From a modeller's point of view, it is natural to try to obtain as simple a relation between relevant parameters as possible. An example of this is the parametrization of the neutral drag coefficient C_{DN} as a function of just one parameter, wind speed, e.g. Edson (2008). As shown by Fairall et al. (2009), there is a strong consistency in the mean between drag coefficient estimates as a function of wind speed for three extensive datasets, but the scatter is considerable. This is a valid approach provided the scatter can be considered as 'random', in the sense that there is no systematic relation between the stress or drag and some parameter other than wind speed. If this is not true, it may lead to systematic and substantial non-linear effects.

One candidate for such possible systematic effects is swell, which has attracted much attention recently. Several studies have made use of reanalysis datasets to explore the world-wide climatology of swell, e.g. Semedo et al. (2011), who demonstrate how swell dominates most parts of the world's oceans. Several theoretical (notably Sullivan et al. 2008) and experimental studies have investigated weak wind situations (U_{10} typically $<2\,\mathrm{m\,s^{-1}}$), where upward momentum transfer has been reported, e.g. Smedman et al. (1994), Grachev and Fairall (2001), and Grachev et al. (2003). There is, however, relatively little known about how the wave field interacts with the lower atmosphere in swell situations with slightly higher wind speeds. Figure 1 illustrates how the drag coefficient C_D (later we will explain why a 'neutral' counterpart is meaningless in swell-dominated situations) plotted as a function of the 10-m wind speed differs widely for swell data in the range $2\,\mathrm{m\,s^{-1}} < U_{10} < 6\,\mathrm{m\,s^{-1}}$ between, on the one hand, data from the Baltic Sea, with observed swell significant wave heights, $H_s \approx 0.3$ m, and on the other hand data from three oceanic sites with H_s in the range of 0.5–2 m. For the sake of completeness, C_{DN} data from the Baltic Sea for cases with growing seas and mixed sea conditions respectively, are also included. All data in Fig. 1 represent unstable thermal conditions (i.e. they have an upward directed kinematic flux of virtual potential temperature).

The present paper aims at a systematic comparison of features relevant to the air–sea exchange regime observed at a trade-wind site outside Oahu, Hawaii and at the Östergarnsholm site in the Baltic Sea. In a later paper, the mechanism of swell/wind wave-interaction will be explored. The trade-wind data are from the rough evaporation duct (RED) experiment (Anderson et al. 2004), which was conducted from late August to mid-September 2001. The data used here were collected on the R/P floating instrument platform (FLIP), moored about 10 km off the north-eastern coast of Oahu in about 370 m of water. As outlined in some detail below, data from meteorological instruments at four levels and wave staffs are used in the analysis.

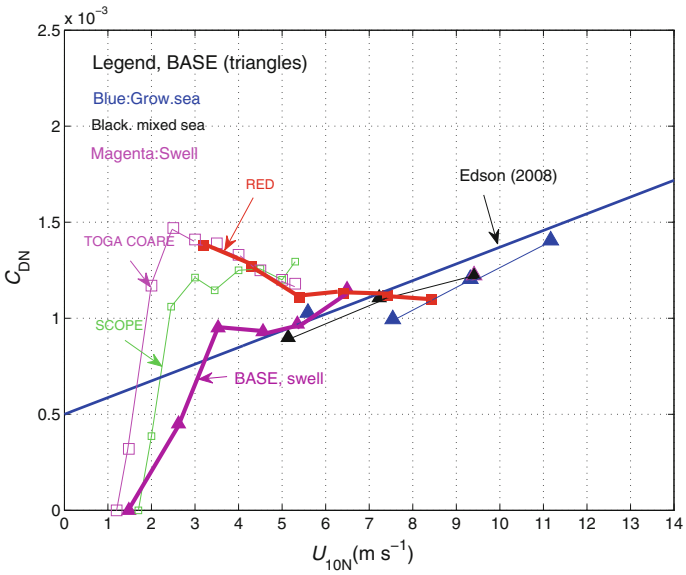

Fig. 1 C_{DN} for respectively unstable growing sea and mixed sea conditions from BASE and C_D for swell data and unstable conditions from BASE, RED, SCOPE and TOGA COARE respectively. All data are velocity bin averages (in some cases the 1.0 m s^{-1} bin, in other cases the 0.5 m s^{-1} bin). The data from SCOPE and TOGA COARE are taken from curves of stress versus wind speed in Grachev and Fairall (2001)

The Baltic Sea data are from the joint U.S.–Swedish–Finnish Baltic Sea swell experiment (BASE) conducted at and around the Meteorological Institute, Uppsala University group (MIUU) tower in September–October 2003, cf. Högström et al. (2008). Turbulence measurements were made at two levels on an air–sea interaction spar (ASIS) buoy and at three levels on the MIUU tower, see below for details.

2 Sites, Instrumentation and Data Selection

2.1 The RED Experiment

The FLIP as moored for the RED experiment is shown in Fig. 2 of Anderson et al. (2004), where the keel was aligned into the prevailing north-easterly trade-wind direction. Its port boom, extending 17 m in a northerly direction, was fitted with a vertical mast, equipped with sensors for meteorological measurements at several heights. For the present study, 50 Hz data of the velocity components and temperature at heights 5.1, 6.9, 9.9 and 13.8 m are used together with measurements of surface elevation (50 Hz) and surface temperature. Data were averaged over successive 30-min periods (denoted 'runs' below). All turbulence signals were subjected to linear de-trending before further processing. Wind fluctuations and sonic temperature fluctuations were measured with Campbell CSAT3 sonic anemometers, temperature with Hart thermistors and surface elevation with four wave-staffs (SIO Wave wire).

The dataset used in the present study begins on 2 September 2001 and ends early on 15 September 2001. It was screened for erroneous data in wind speed, momentum

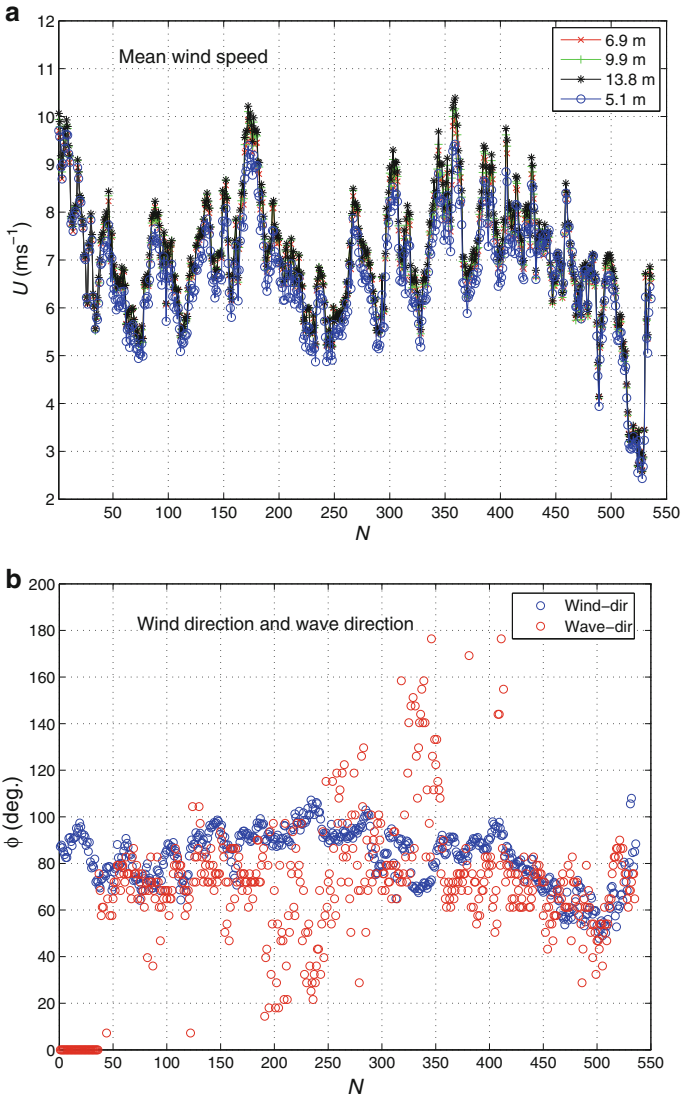

Fig. 2 Time plots of various parameters from RED. In all sub-plots N = data number. **a** Mean wind speed at four levels; **b** Wind direction, ϕ, and direction of dominant waves (swell); **c** $\langle uw \rangle \equiv \overline{u'w'}$ at four levels; **d** The temperature difference between the surface and 10 m; **e** Significant wave height; and **f** wave age, c_p/U_{10}. The line corresponds to $c_p/U_{10} = 1.2$

flux and sensible heat flux at the four levels. Numerous spikes were found in the data plots of all signals, though fortunately it is possible to remove most spikes and replace the corresponding data with interpolated values. Wave data were also screened in a similar way. Most of the time, significant wave height and peak wave frequency obtained from each of the four wave-staffs, agreed very well, so it was mostly straightforward to identify erroneous segments. After this screening, 536 of the original 546 30-min 'runs' remained. Most of the ten 'runs' that were removed because of several

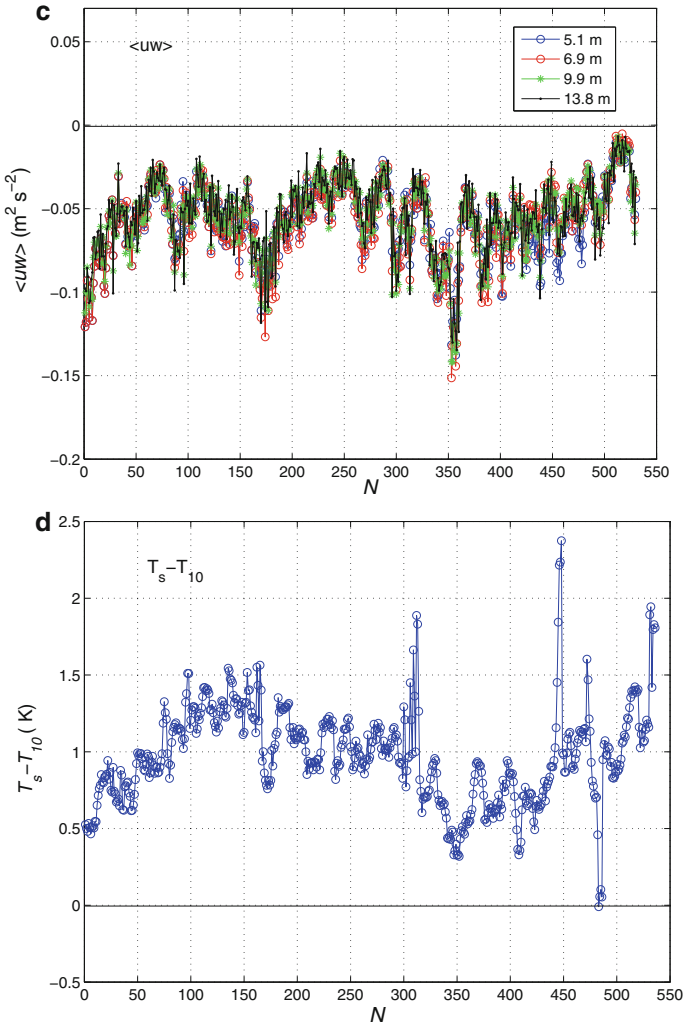

Fig. 2 continued

obviously erroneous values happened to occur during the only day when precipitation occurred.

The surface elevation data have been processed to give both one-dimensional (1D) and 2D spectral plots for each run. Meteorological data have been processed to give energy spectra for the u, v and w components (respectively the horizontal along-wind, cross-wind and vertical components) as well as uw cospectra and quadrature spectra, which will be extensively used in a forthcoming paper.

2.2 The BASE Data

The Östergarnsholm site and the instrumentation employed during the BASE experiment are described in detail in Högström et al. (2008), so here only a brief summary is given. This

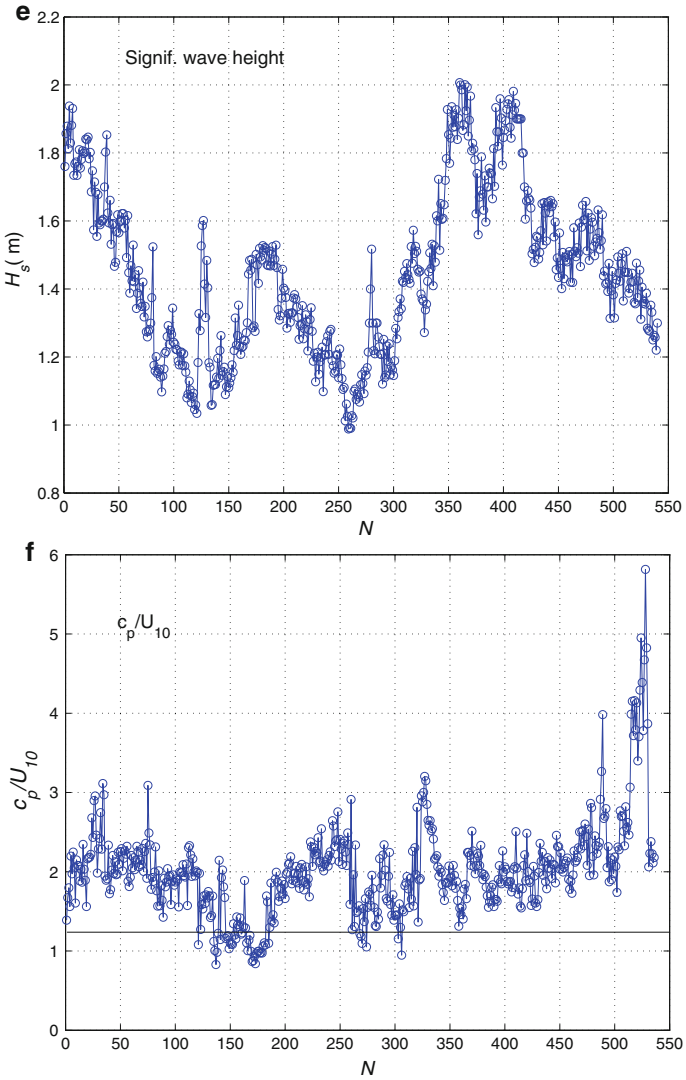

Fig. 2 continued

reference also contains a map of the experimental area. The Östergarnsholm station has been operated on a semi-continuous basis since 1995 and analysis of the data has been reported in, e.g., Smedman et al. (1997, 2009) and Högström et al. (2009).

The instrumented 30-m high tower is located on land but close to the water and with a wide sector (winds from ≈080°–220°) over unobstructed water, with more than 100 km of fetch. The base of the tower is at 1.3 m above mean sea level, which varied within ±0.2 m during the experiment, and at a distance of a few tens of m from the water in the relevant sector. The tower is equipped with Solent 1012 sonic anemometers (Gill Instruments, Lymington, UK) at 10, 18 and 26 m above mean sea level, with data from these instruments recorded at 20 Hz. Slow response ('profile') sensors for wind speed, direction and

temperature measurements are placed at 8.1, 13.1, 15.5, 21.5 and 30.0 m nominal heights above sea level.

In Smedman et al. (1999) it was concluded that the measurements from the selected sector were likely to be largely unaffected by the tower's location on the island's edge. In Högström et al. (2008) this conclusion was further substantiated by comparisons with simultaneous data from the ASIS buoy, which was anchored 4 km further offshore. A footprint calculation for the measurements was carried out showing that the tower flux measurements "see" areas far enough removed from the shore that shoaling effects of waves observed during the experiment are unlikely to affect the measurements. This conclusion is important for the inter-comparison with the data from the RED experiment, because it means that possible differences found are likely to be due to fundamental differences in the air–sea exchange regime in the enclosed Baltic Sea compared to that of the oceanic site of the RED experiment and not to any local effects such as shoaling.

Four km to the south-east of the tower an instrumented ASIS buoy (Graber et al. 2000) was anchored in 36-m deep water. The buoy itself (Fig. 2 in Högström et al. 2008) can be described as a pentagonal cage of slender cylinders with an open deck about 1 m above the water, which is the base of a slender 4.5 m open lattice mast. The mast was equipped with Gill R2A sonic anemometers at 2.56 and 5.3 m above the water surface, while mean wind speed and direction were measured with Vaisala WM301 cup anemometers at 2.42 and 1.18 m (part of the experiments only). Air temperature was measured at 0.7 and 1.7 m above the water using aspirated copper–constantan thermocouples. An array of 3.3 m long, 9×10^{-4} m diameter capacitance wave gauges, arranged in a 0.93-m radius centered pentagon, measured surface elevation. Platform motions were recorded with a system of three orthogonally mounted rate gyros (Systron Donner GC1) and a tri-axis accelerometer (Columbia Research Laboratory SA-307HPTX) in a watertight housing 7.7 m below the water surface, see Drennan et al. (2003) and Pettersson et al. (2003) for descriptions of the processing of ASIS data.

All data from the Östergarnsholm station and the ASIS buoy were evaluated as 30-min 'runs' and put together into a fully synchronized data base. All turbulence data were subject to linear de-trending before further processing, while all data were screened for possible errors, including occasional flow distortion from the masts. A final dataset, for winds from the sector 080°–220°, ASIS operating without flow distortion, and obvious erroneous data removed, contained 750 half-hour 'runs'.

3 Prevailing Meteorological and Wave Conditions During the RED and BASE Experiments

Figure 2 shows, in six panels, a number of relevant parameters from the RED experiment. The 10-m wind speed (Fig. 2a) is between 5 and 10 m s^{-1} most of the time, with one period near the end of the time series having $U_{10} \approx 3$ m s^{-1}. The wind direction (Fig. 2b) is between 050° and 110°; this panel also shows the prevailing peak wave direction, which for most of the time is fairly close to the wind direction but which, on occasions, differs from the wind direction by as much as 90°. As discussed below, it is sometimes difficult to uniquely define a 'wave direction' because the wave field is dominated by multiple swell systems with widely different directions. The streamwise momentum flux $\overline{u'w'}$ is plotted for all four measuring heights in Fig. 2c, and is seen to be roughly constant with height. In fact, for individual 30-min runs, the variation is typically less than ±5%. The temperature difference between the surface and 10 m (Fig. 2d), is always positive and mostly in the range 0.5–1.5 K i.e. the atmosphere is always slightly unstable. The significant wave height (Fig. 2e) varies between

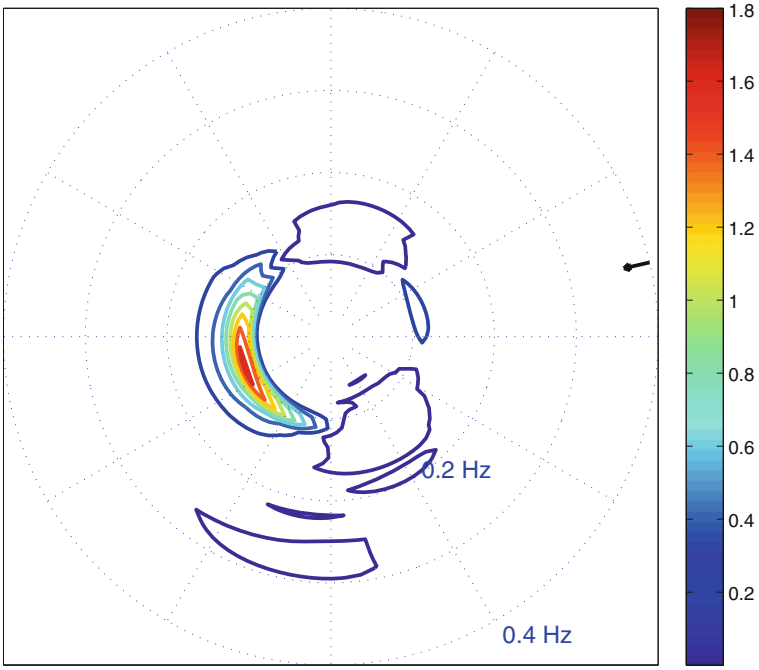

Fig. 3 Example of a two-dimensional wave spectrum from RED. *Black arrow* at the right-hand side indicates wind direction. $H_s = 1.33\,\mathrm{m}$, $c_p/U_{10} = 4.66$, $U = 3.22\,\mathrm{m\,s^{-1}}$

1.0 and 2.0 m, the wave field being dominated by swell, cf. Fig. 2f, which shows that the wave age c_p/U_{10} (where c_p is the peak wave phase speed) is typically in the range 1.5–2.5, being below the swell limit of 1.2 only for 7% of the time. Note that c_p/U_{10}-values between 3.5 and 5.5 occur during the period previously (Fig. 2a) observed to have about $3\,\mathrm{m\,s^{-1}}$ wind speed.

The wave field can be represented in a two-dimensional, polar representation, see Fig. 3, where surface elevation isolines are plotted as function of wave direction and frequency (length of the radius vector). The example in Fig. 3 is from the weak wind period ($U_{10} = 3.2\,\mathrm{m\,s^{-1}}$), which implies that swell dominates, with three distinct maxima at frequencies in the range 0.1–0.15 Hz, which correspond to wavelengths in the approximate range 70–160 m. The maximum that corresponds to waves travelling from a roughly north-easterly direction dominates in this example and in most individual plots from the RED experiment, irrespective of wind speed. This is clearly swell related to the prevailing trade wind. The two other, smaller, maxima represent respectively swell originating probably from storms in the northern Pacific, and waves arriving from the south—apparently noise, as the swell is from the direction of the island of Oahu.

By integrating over all directions, 1D wave spectra that are functions only of frequency, n, are obtained. Figure 4 shows, in a log–log representation, a typical measured wave spectrum for a particular case with $U_{10} = 7.0\,\mathrm{m\,s^{-1}}$, which is the mean wind speed for the RED experiment. The wave age c_p/U_{10} for this case is 2.09. For frequencies above $\approx$0.3 Hz, spectral energy $S(n)$ falls off as $n^{-4.8}$, which corresponds to a straight line of slope -4.8 in this representation. The low-frequency fall-off can also be approximated by a straight line, and a schematic spectrum consisting of these two lines is shown in Fig. 5. This also includes the Pierson–Moskowitz (PM) spectrum for a fully-developed sea and $U_{10} = 7.0\,\mathrm{m\,s^{-1}}$, derived

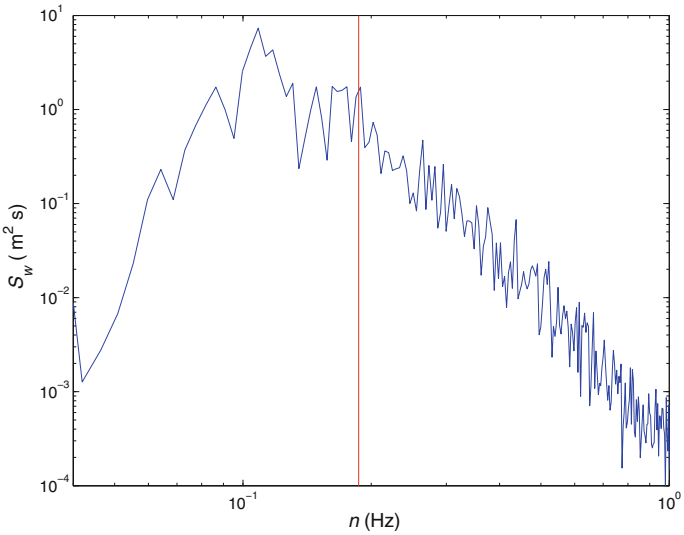

Fig. 4 The 1D wave spectrum, S_{w}, in a situation (11 September 2001, 1453 local time) with $U_{10} = 7.0\,\mathrm{m\,s^{-1}}$, $H_{\mathrm{s}} = 1.99$ m and $c_{\mathrm{p}}/U_{10} = 2.09$. The *red line* indicates the frequency n_0 defined by the requirement that the corresponding wave phase speed $c_0 = 1.2U_{10}$, which gives $n_0 = 0.83g/(2\pi U_{10})$

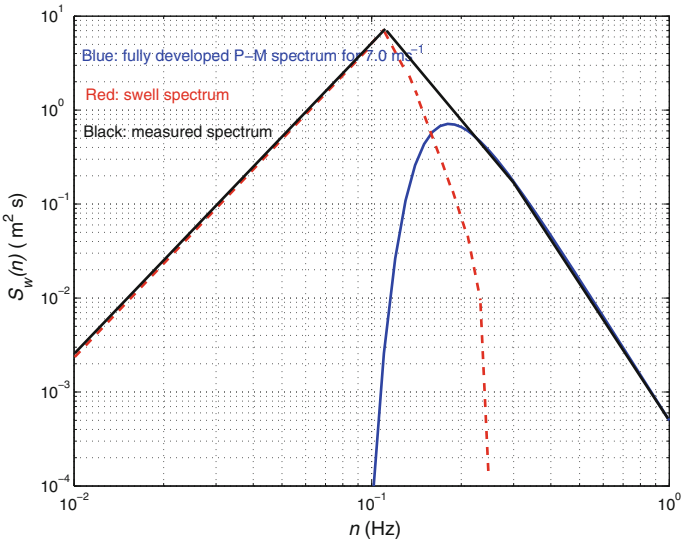

Fig. 5 Example of a 1D wave spectrum from RED (*black*), with Pierson–Moskowitz-spectrum (*blue*) derived for fully developed seas (constants according to Holthuijsen 2007, Sect. 6.3.3). The measured wave spectrum in Fig. 4 has been approximated with three *straight lines* in this log–log representation. The *dashed curve in red* is the difference between this 'observed' (but slightly idealized) spectrum and the Pierson–Moskowitz spectrum

with the constants suggested by Holthuijsen (2007). It fits the observed high-frequency spectrum very well. A resulting 'swell-spectrum' has been derived graphically by subtracting the PM spectrum from the observed spectrum, the dashed curve.

Table 1 The BASE experiment

Wave age	Unstable			Stable
	$c_p/U_{10} < 0.8$	$0.8 < c_p/U_{10} < 1.2$	$c_p/U_{10} > 1.2$	
Number of data	185	175	186	204
$\langle U_{10} \rangle$ (m s^{-1})	8.5	7.9	4.9	10.1

Number of unstable and stable data; the unstable data are subdivided according to wave age. Also, $\langle U_{10} \rangle$ (m s^{-1}) is the mean 10-m wind speed for each unstable category

Whereas the RED experiment, as illustrated above, represents conditions during typical trade-wind conditions, with wind speeds of moderate magnitude from a narrow sector, a slightly unstable atmospheric boundary layer (ABL) and ever-present swell of 1–2 m height typically travelling in the mean wind direction, the data from the BASE experiment represent a very different regime, typical of mid-latitude conditions (alternating low pressure and anti-cyclonic conditions). As a result, thermal stability in the lower ABL varied between unstable and stable conditions, and the wave age varied from that of a growing sea, $c_p/U_{10} < 0.8$, to that of swell, $c_p/U_{10} > 1.2$, as summarized in Table 1.

In fact, Table 1 shows that, during unstable conditions, growing sea ($c_p/U_{10} < 0.8$), mixed sea ($0.8 < c_p/U_{10} < 1.2$) and swell ($c_p/U_{10} > 1.2$) conditions respectively, each occurs for about 25% of the time. Wave classification was not made during stable conditions, which also occur during about 25% of the time. Note that, for BASE, the mean 10-m wind speed for all categories except swell is fairly high, in the range 8–10 m s^{-1}, while for swell conditions the mean wind speed is ≈4–5 m s^{-1}.

4 Results

4.1 Features that are Similar During the RED and BASE Experiments

All 1D wave spectra were divided into two parts, $E1$ and $E2$ respectively, where $E1 + E2 =$ total wave energy and $E1$ contains the long waves and $E2$ the short waves (Smedman et al. 2003). The separation between the two parts is at the frequency n_0 defined by the requirement that the corresponding wave phase speed $c_0 = 1.2U_{10}$ (Pierson and Moskowitz 1964). For deep water, we have $c = g/2\pi n$ (se e.g. Holthuijsen 2007), so that

$$n_0 = 0.83g/(2\pi U_{10}). \tag{1}$$

Because of the observation (Fig. 8) that the wind speed is constant at heights <7 m above the water, it would be consistent to have the original constant value suggested by Pierson and Moskowitz (1964) 0.88 instead of 0.83, but in practice this will not influence the results to any measurable degree, so we chose 0.83 here.

For the spectrum shown in Fig. 4, n_0 defined by Eq. 1 is indicated, and roughly separates swell waves to the left of the line and local wind waves to the right. Figure 5 represents spectral energy as well as frequency on logarithmic scales. In a linear representation, the area under the spectral curve to the left of the line $n = n_0$ gives $E1$ and the corresponding area to the right $E2$.

In steady conditions, when the high-frequency part of the spectrum is fully developed, the high-frequency part of the spectrum, $E2$, is expected to be a function of the local wind

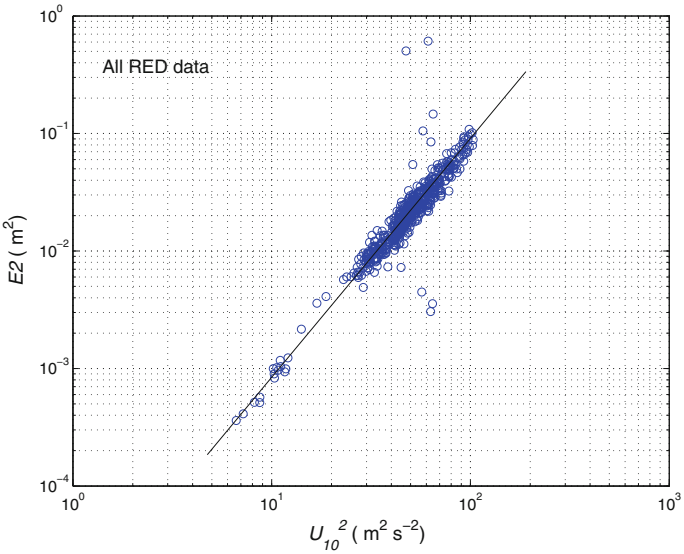

Fig. 6 High-frequency wave-spectral fraction $E2$, i.e. the integral of the wave spectrum $\int_{n_0}^{\infty} S_{\mathrm{w}}(n)\mathrm{d}n$ where n_0 is defined by the requirement that the corresponding wave phase speed $c_0 = 1.2U_{10}$, giving $n_0 = 0.83g/(2\pi U_{10})$

speed only. This is clearly demonstrated for the RED experiment in Fig. 6, which shows, in a log–log representation, all RED $E2$ data (where $E2 = \int_{n_0}^{\infty} S(n)\mathrm{d}n$), and where $S(n)$ is the wave spectral energy) plotted against U_{10}^2. Regression gives the result

$$E2 = 10^{-3}U_{10}^4/g^2, \tag{2}$$

which agrees with the dimensionless energy of the fully developed sea (Pierson and Moskowitz 1964).

Exactly the same result was obtained by Smedman et al. (2003) who carried out a similar analysis on a dataset from the Östergarnsholm tower (measurements obtained during the time period 1995–2001), their Fig. 2a. This is also the case for measurements obtained from an ASIS buoy during three recent oceanic field experiments: FETCH (Flux, État de la mer et Télédétection en Condition de fetch variable), Gasex01 (GasExchange Experiment 2001) and the Southern Ocean Gas Experiment, SOGasex (Sahlée et al. 2012).

The swell data for the BASE experiment were divided according to 10-m wind speed into four 1 m s^{-1} bin cases, and mean wind profiles for each case are shown in Fig. 7. Most remarkable are the features of the case 1 profile: the wind speed increases to a maximum at a height of 7–8 m, decreasing slightly for higher levels. Similar wind profiles were obtained for the two low wind (1.5 m s^{-1}) cases C1 and F1 of Smedman et al. (2009), their Fig. 3a, where the wind-speed maximum is even more pronounced. The other wind profiles in Fig. 7, i.e. those for Cases 2, 3 and 4, all have large vertical gradients below a height of 7–8 m and almost constant wind speed at higher levels.

Figure 8 shows corresponding 1 m s^{-1} bin mean wind profiles for the RED experiment. Considering that the number of measurement levels are fewer here, the agreement in wind-profile shape between the data from the RED (Fig. 8) and BASE experiments (Fig. 7) is remarkable. All the profiles from the RED experiment have a lower part, below 7 m, with a

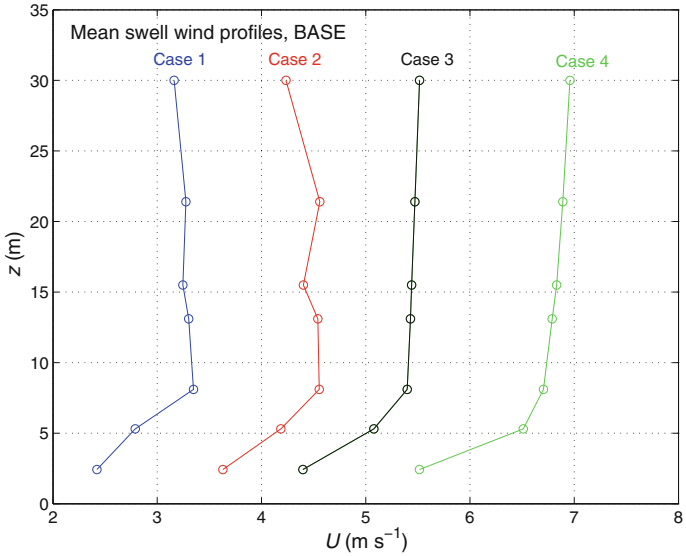

Fig. 7 Mean swell wind profiles from BASE for wind-speed bins with mean values respectively: case 1: $U_{10} < 4\,\mathrm{m\,s^{-1}}$; case 2: $4\,\mathrm{m\,s^{-1}} < U_{10} < 5\,\mathrm{m\,s^{-1}}$; case 3: $5\,\mathrm{m\,s^{-1}} < U_{10} < 6\,\mathrm{m\,s^{-1}}$; and case 4: $6\,\mathrm{m\,s^{-1}} < U_{10} < 7\,\mathrm{m\,s^{-1}}$

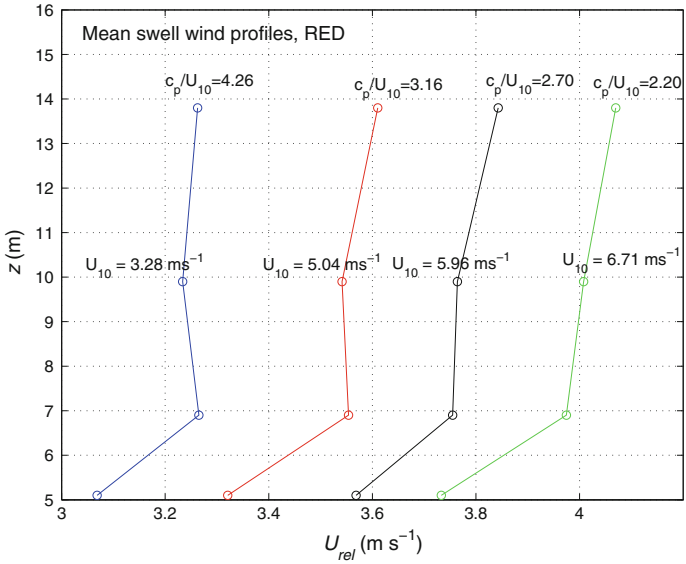

Fig. 8 Mean swell wind profiles from RED for wind-speed bins with mean values respectively: 3.28, 5.04, 5.96 and $6.71\,\mathrm{m\,s^{-1}}$. Note that the profiles have been displaced along the x-axis (in order to stress the shape of each individual profile) so that the U values are relative

large gradient and an upper part with close to zero gradient. Note, in particular that the profile denoted $3.28\,\mathrm{m\,s^{-1}}$ for the RED data has a slight maximum at virtually the same height, near 7 m, as the corresponding profile from the BASE experiment. A similar feature was also

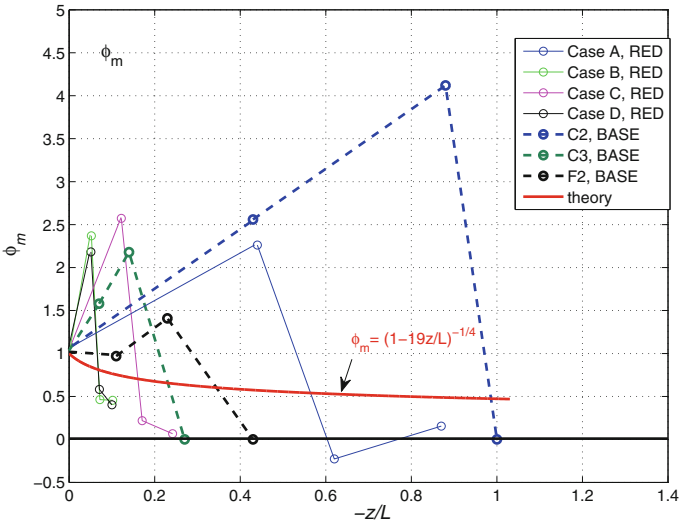

Fig. 9 ϕ_{m} plotted against $-z/L$. The *red curve* is from Högström (1996) and is based on data from several over land studies. The other *curves* are for swell cases from RED and BASE, according to the legend

obtained by Sullivan et al. (2008) in their large-eddy simulation (LES) of flow over idealized swell waves, although the height of the wind maximum was greater, a result that may well be a numerical artifact of the LES close to the surface. They explain that this is the result of upward momentum transfer by the swell waves, a feature also obtained in analytic studies of the same problem, see Hanley and Belcher (2008) and Semedo et al. (2009). Analysis of the turbulence kinetic energy (TKE) budget based on data from the RED experiment and presented below, shows that upward pressure transport of TKE does indeed occur (together with a corresponding downward transport of larger magnitude below 7 m).

In Högström et al. (2009) it was noted that Monin–Obukhov scaling (MO scaling) does not apply for the five swell cases studied there, supporting earlier conclusions of Drennan et al. (1999). Figure 9 shows

$$\phi_{\mathrm{m}} = \left(\frac{kz}{u_*}\right)\frac{\partial U}{\partial z} \tag{3}$$

against z/L, where z is height (m), k is the von Karman constant $= 0.40$, u_* is the friction velocity $= \sqrt{-(\overline{u'w'})_0}$, and L is the Obukhov length, defined as

$$L = -\frac{u_*^3 T_0}{gk\overline{w'\theta_{\mathrm{v}}}}, \tag{4}$$

where T_0 is a mean surface-layer temperature (K), g is the acceleration due to gravity (m s^{-2}) and $\overline{w'\theta_{\mathrm{v}}}$ is the kinematic vertical flux of virtual potential temperature (m s^{-1}K).

The red curve in Fig. 9 represents the equation of Högström (1996):

$$\phi_{\mathrm{m}} = (1 - 19z/L)^{-1/4}, \tag{5}$$

which was derived from several field experiments over land for unstable conditions, i.e. $z/L < 0$. The other curves in Fig. 9 are derived from the measurements during the RED experiment (solid line curves) and during the BASE experiment (dashed lines) respectively.

Table 2 Selected cases from the RED experiment

Case	Number of 30-min runs	U_{10} (m s^{-1})	H_s (m)	c_p/U_{10}	u_* (m s^{-1})	Swell wavelength (m)
A	16	3.2	1.36	4.20	0.114	111
B	8	8.0	1.90	1.90	0.267	142
C	16	6.1	1.20	2.19	0.204	112
D	12	9.6	1.48	0.96	0.310	55

For the RED experiment, data from four cases of 4–8 successive hours of reasonably stationary conditions are included, cf. Table 2; the BASE curves are from the three swell cases studied in Smedman et al. (2009) and Högström et al. (2009) (their C2, C3 and F2) that have $u_* > 0$. ϕ_m was evaluated with Eq. 3, where u_* was obtained using eddy-correlation measurements of $\overline{u'w'}$ (which is very close to height constant in each case) and measurements of U at two consecutive levels, giving the approximation:

$$\frac{\partial U}{\partial z} \approx \frac{U(z_2) - U(z_1)}{z_2 - z_1}, \tag{6}$$

and valid at $z_m = (z_1 + z_2)/2$. The Obukhov length was evaluated with Eq. 4 from eddy-correlation measurements of $u'w'$ and the heat flux $\overline{w'\theta_v}$ (which is also close to constant with height).

If MO theory was indeed valid, we would have expected the measurements to fall on (or scatter randomly around) the red curve or any other single curve, which is unity at the surface (i.e. for $z/L = 0$), decreasing monotonously with z/L. It is evident from Fig. 9 that this is definitely not the case for the RED and the BASE swell measurements. Instead, there are individual ϕ_m curves for each case shown, which all first increase from unity to values in the range 1.5–4, then suddenly decrease to values around zero. It is noteworthy that this result is also valid for the RED case, denoted D, which has a mean wind speed as high as 10 m s^{-1} and $c_p/U_{10} = 0.96$. As this was the maximum mean wind speed measured during the RED experiment, we cannot make any prediction about the upper limit of validity of this 'non-MO-regime'. Probably the swell magnitude is the key factor.

It is worth noting that $\overline{u'w'}$ is very nearly constant with height during the RED experiment, typical deviations at the four measurement heights from the mean being ±5% or less. Also the flux of sensible heat, $\overline{w'\theta'}$ is found to be close to height constant. Thus one of the requirements for MO theory to apply is indeed satisfied. This is, however, a necessary, but not a sufficient, criterion. For MO theory to be valid, it is necessary that the only relevant length scales are the height above the ground, z, and the Obukhov length, L, defined by Eq. 4. The result displayed in Fig. 9 shows that, in cases where swell plays an important role for the lower boundary conditions, the turbulent structure of the surface layer is strongly influenced in a way not accounted for in MO theory. What makes ϕ_m deviate from MO theory is the fact that the wind-speed gradient, $\partial U/\partial z$, varies in a manner very different compared to that expected, being very large below about 7 m and close to zero above.

In Högström et al. (2009) the TKE budget was studied for five cases with swell. Methods similar to those developed in that paper have been applied to derive TKE budgets for the four cases from RED listed in Table 2. The equation for the TKE budget reads:

$$\underset{Trc}{\frac{\partial \overline{q'^2}}{2\partial t}} + \underset{Adv}{\overline{\vec{U} \cdot \nabla \left(\frac{q'^2}{2}\right)}} = \underset{P}{\overline{u'w'}\frac{\partial U}{\partial z}} - \underset{B}{\frac{g}{T}\overline{w'\theta'_v}} + \underset{T_t}{\frac{\partial}{\partial z}\frac{\overline{w'q'^2}}{2}} + \underset{T_p}{\frac{1}{\rho}\frac{\partial \overline{p'w'}}{\partial z}} + \varepsilon \tag{7}$$

where the instantaneous TKE $q'^2/2 = 0.5(u'^2 + v'^2 + w'^2)$, where u', v' *and* w' are instantaneous deviations of, respectively, the longitudinal, the lateral and vertical wind components from their respective mean values, $\vec{U}$ is the horizontal wind vector, U is the magnitude of the mean wind, which varies with height z, T mean temperature of the surface layer in kelvin, θ'_v is the instantaneous deviation of virtual temperature from its mean, ρ is air density, p' is the instantaneous deviation of air pressure, ε is the molecular rate of dissipation of TKE. The overbar represents an average, in the present study a time average over 30 min. Each of the terms in (7) was evaluated separately for every 30- min period, and a 'case-average' was then derived.

In (7) all terms except T_p and *Adv* can be evaluated directly from the simultaneous turbulence measurements at four levels above mean water level. *Adv* was evaluated during BASE and shown to be small; it is neglected here. In addition, for the derivation of the term P, mean wind data from several levels (see below) are required. The remaining term, T_p is derived as a residual. The evaluation procedures adopted for the terms, P, B, T_t and ε are briefly outlined below. For more details, see the Appendix.

1. Turbulence production, $P = \overline{u'w'}\frac{\partial U}{\partial z}$

This term is evaluated from measurements of the covariance, $\overline{u'w'}$, and mean wind-speed gradient at each 'turbulence level' (5.1, 6.9, 9.9 and 13.8 m respectively). In addition, since we wish to extend the TKE analysis down to the water surface, the following procedure is adopted. The approximate wind-speed gradient at 5 m is known; near the surface, we expect the wind profile to approach the logarithmic law, so that $\partial U/\partial z = u_*/kz$, where u_* is obtained from the eddy-correlation measurements of $\overline{u'w'}$. As shown in the Appendix, a second-order polynomial in log z is a reasonable approximation for the wind profile for $z_1 \leq z \leq 5.1$m, where z_1 is of the order O (1 m); in particular, it is likely to give a good approximation to the mean wind gradient (which is the quantity needed in Eq. 7) in this layer.

2. The buoyancy term, $B = -\frac{g}{T}\overline{w'\theta'}_v$

This term requires only the 'raw' measurements of turbulent flux of virtual temperature, which is very nearly equal to the corresponding flux of 'sonic' temperature, obtained directly from the sonic measurements at each 'turbulence level', and estimates of the mean temperature at each level.

3. The turbulent transport term, T_t can be written:

$$T_t = (1/2)\frac{\partial}{\partial z}(\overline{w'u'^2} + \overline{w'v'^2} + \overline{w'^3}) = \frac{\partial \overline{w'E'}}{\partial z},$$

where each of the three third-order terms $\overline{w'u'^2}$, $\overline{w'v'^2}$ and $\overline{w'^3}$ is obtained from the turbulence measurements at the four 'turbulence levels', and their sum is plotted against height as well as their respective standard deviations. This enabled approximate best fit curves to be drawn manually, and from these curves, in turn, approximate derivatives to be obtained. The inherent uncertainty in this procedure is acceptable because the magnitude of the T_t term is an order of magnitude less than that of the leading terms (P, ε and T_p).

4. Dissipation, ε.
Power spectra for the u component pre-multiplied by frequency, $nS_u(n)$ were plotted on a log–log scale against frequency n for all 30- min data of the four cases and heights. According to Kolmogoroff (1941), and further assuming Taylor's hypothesis to be valid, the spectral curves in the inertial sub-range are expected to be straight lines with $-2/3$ slope in this representation

$$nS_u(n) = \alpha_1 \varepsilon^{2/3} (2\pi n/U)^{-2/3}, \tag{8}$$

so that

$$\varepsilon = \frac{2\pi n}{U} \left(\frac{nS_u(n)}{\alpha_1} \right)^{3/2}. \tag{9}$$

Here α_1 is a universal constant ≈ 0.50 (cf. Högström 1990) and n must be chosen in the region with the $-2/3$ slope. As shown in the Appendix, the near-neutral prediction for the dissipation $\varepsilon = u_*^3/kz$ can be used near the surface to match the data derived with (9). Details of the evaluation are given in the Appendix.

5. The pressure transport term, T_p
Since the left-hand side terms in Eq. 7 are much smaller than the right-hand side terms (see Appendix and below), the pressure transport T_p, can be calculated as the residual, i.e. as minus the sum of the terms P, B, T_t and ε.

Figure 10a–d shows the result of the TKE calculations for the four selected cases from the RED experiment (Table 2) and, for comparison, one case, Fig. 10e, from BASE. It is clear in all four cases that mechanical and buoyancy production, i.e. $P + B$, does not match dissipation plus turbulence transport, $\varepsilon + T_\mathrm{t}$. The difference is the 'measured' pressure transport, $T_\mathrm{p} = (T_\mathrm{p})_\mathrm{tot}$; this term is positive (a loss) for $z < 7$ m, but for all four cases it changes sign at around 7 m. Below 2 m this term is negative again. As was done in Högström et al. (2009), for the swell cases from BASE denoted C2, C3 and F2, it is natural to interpret T_p as the sum of an exponentially decreasing negative term, which fits the T_p curve from 7 to 8 m upwards, and a positive term, for $z < 7$ m, $(T_\mathrm{p})_\mathrm{s}$, caused by the relatively short waves. As in Högström et al. (2009), the interpretation is that the negative, exponentially decreasing part, $(T_\mathrm{p})_\mathrm{exp}$, represents the upward transport of momentum from the swell waves (caused by form drag) and the positive part $(T_\mathrm{p})_\mathrm{s}$ is the downward transport of momentum related to relatively short waves, i.e. for waves with a phase speed less than the wind speed above the 'knee' observed in the swell wind profiles of Fig. 8.

Figure 10a is the TKE result for RED case A, which has $U_{10} = 3.2\,\mathrm{m\,s^{-1}}$. It is similar to Fig. 2c in Högström et al. (2009), which is a case with $U_{10} = 4.0\,\mathrm{m\,s^{-1}}$, which is reproduced here as Fig. 12e. In Högström et al. (2009) a detailed error analysis was performed, with the conclusion: "The error in T_p is $\pm 50\%$, so the TKE plots are, in a sense, only semi-quantitative, but there are no reasons to expect them to be systematically biased". In essence, this conclusion is valid in the present analysis as well. Thus, we conclude that the TKE budgets of the BASE and RED experiments are on the whole similar.

4.2 Features that are Dissimilar During the RED and BASE Experiments

Figure 1 is a composite plot of the drag coefficient as a function of U_{10} with data from the BASE and RED experiments as well as from two other oceanic experiments, TOGA COARE (The Tropical Ocean Global Atmosphere Coupled Ocean Atmosphere Response Experiment) and SCOPE (the San Clemente Ocean Probing Experiment). For the BASE experiment, $1\,\mathrm{m\,s^{-1}}$ bin mean values of C_DN or, as the case may be (see below), C_D, for

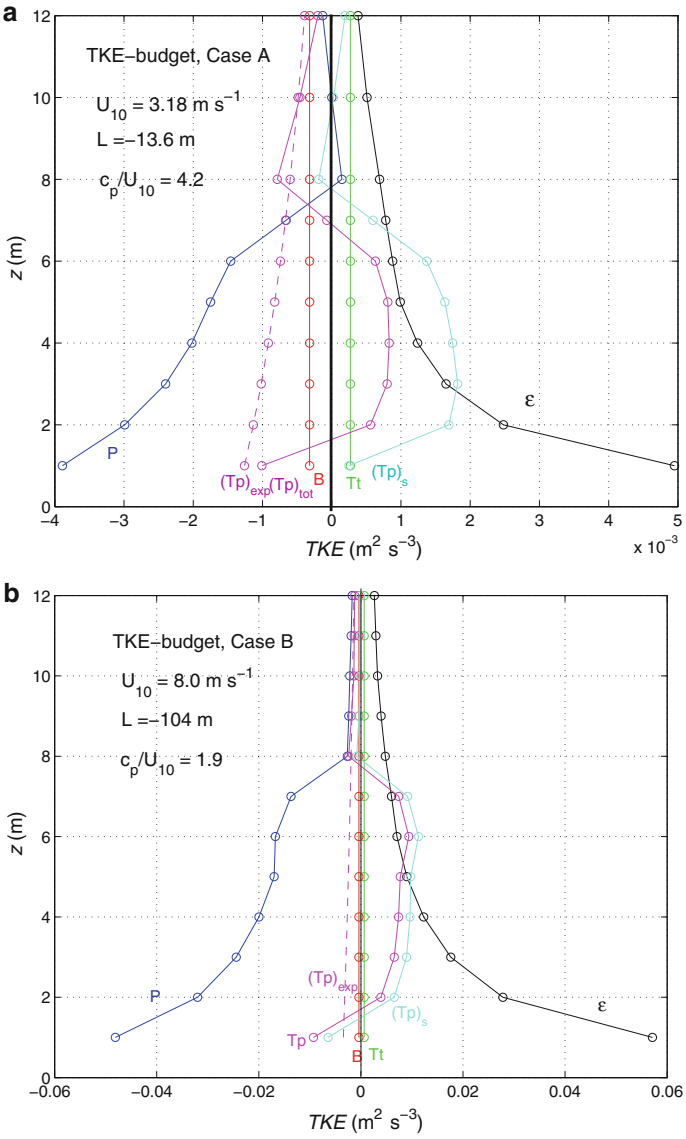

Fig. 10 TKE budgets for four cases from RED, **a, b, c, d**, and one case, **e**, from BASE, plotted as function of height z. P mechanical production; B buoyancy production; T_t turbulent transport; ε dissipation; T_p pressure transport, which in turn has been divided into two parts, so that $(T_p)_{tot} = (T_p)_{exp} + (T_p)_s$, see text for details. All terms have been plotted as function of height above the water, z. **a** Case A from RED; **b** case B from RED; **c** case C from RED; **d** case D from RED; and **e** case C3 from BASE

unstable conditions divided into three categories: growing sea ($c_p/U_{10} < 0.8$), mixed sea ($0.8 < c_p/U_{10} < 1.2$) and swell ($c_p/U_{10} > 1.2$) respectively. For the growing sea and mixed sea, C_{DN} is defined from the expression of C_D in the Monin–Obukhov framework

$$C_D = (u_*/U(z))^2 = k^2/[\ln(z/z_0) - \psi_m(z/L)]^2, \tag{10}$$

with

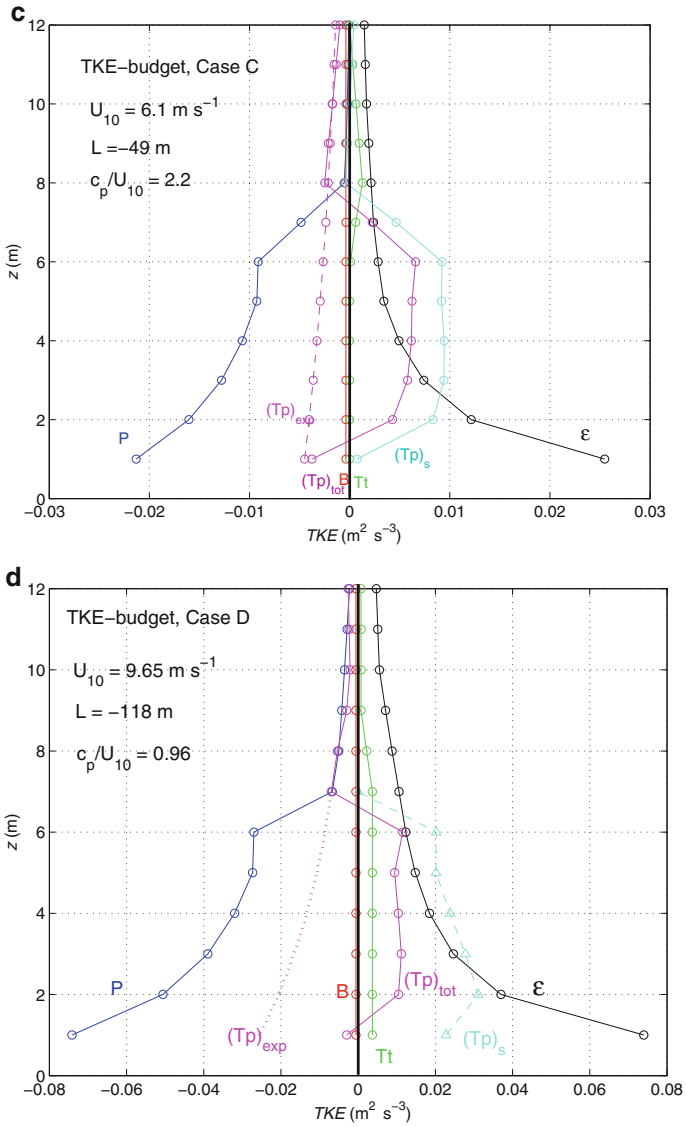

Fig. 10 continued

$$\psi_{\mathrm{m}} = \int_0^{z/L} ([1 - \phi_{\mathrm{m}}(\varsigma)]/\varsigma) d\varsigma, \tag{11}$$

In neutral conditions, $\psi_{\mathrm{m}} = 0$ and

$$C_{\mathrm{DN}} = k^2/[\ln(10/z_0)]^2. \tag{12}$$

For swell-dominated conditions, it is not meaningful to convert measured C_{D} to C_{DN} values since, as shown previously by Drennan et al. (1999) and also herein, MO theory is not valid

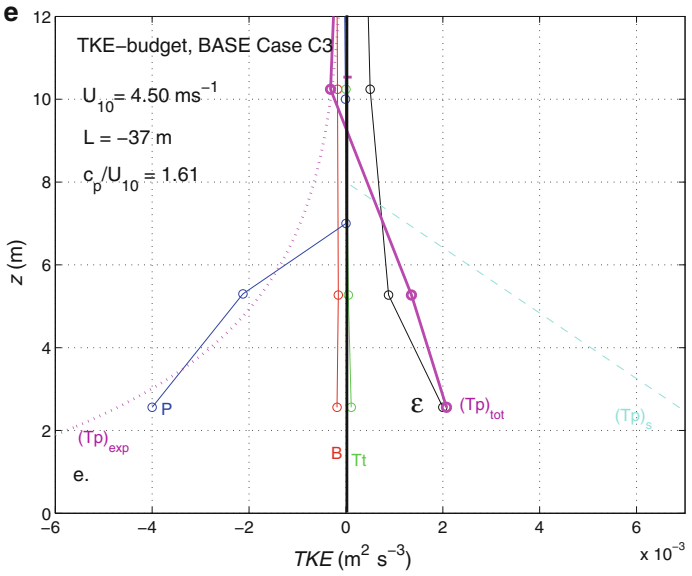

Fig. 10 continued

in these conditions, see also Drennan et al. (2005). Thus, for swell data from BASE and RED, Fig. 1 shows C_D instead of C_{DN}. Also shown in this figure are C_D data from the experiments TOGA COARE and SCOPE. They have been derived from plots of $\tau_x = -\rho_a \overline{u'w'}$ against U, Fig. 1b and c respectively in Grachev and Fairall (2001).

It is clear from Fig. 1 that the BASE data for unstable growing sea and mixed sea conditions are reasonably close to what is obtained from the Edson (2008) parametrization. When we consider the swell data there is, however, a strong systematic deviation for a wide wind-speed range, $2\,\mathrm{m\,s^{-1}} < U_{10} < 6\,\mathrm{m\,s^{-1}}$, between the data from the BASE experiment on the one hand and the data representing oceanic conditions i.e. those from RED, TOGA COARE and SCOPE on the other. The data from the RED experiment agree completely with those from TOGA COARE in this wind-speed range, the SCOPE data agree with RED for $U > 4\,\mathrm{m\,s^{-1}}$. It is a reasonable hypothesis that the magnitude of swell plays a decisive role here. Thus the significant wave height, H_s, in the BASE swell cases was typically 0.3 m (cf. Table 1 of Smedman et al. 2009); in RED $1.0\,\mathrm{m} < H_s < 2.0\,\mathrm{m}$ and in SCOPE (Grachev and Fairall 2001) $0.5\,\mathrm{m} < H_s < 1.0\,\mathrm{m}$; waves were not measured in TOGA COARE, but according to Fig. 2 of Semedo et al. (2011), the climatological mean swell height during the December, January, February period in the area where this experiment took place is about 1.5 m. In a forthcoming paper, the measurements from the RED experiment together with other oceanic data will be used to study the mechanism for the interaction of swell and wind waves.

5 Conclusions

Air–sea interaction data from a site in the Baltic Sea (experiment BASE) and from a trade-wind dominated site outside Oahu, Hawaii (experiment RED) were compared with regard to wind speed and momentum flux features during following and cross-swell conditions (note that we have no observations for counter-swell conditions). During the RED experiment,

the atmospheric stratification was always unstable, and swell dominated almost completely, with the significant wave height in the range $1.0\,\mathrm{m} < H_s < 2.0\,\mathrm{m}$. The wind-speed range was $3\,\mathrm{m\,s^{-1}} < U_{10} < 10\,\mathrm{m\,s^{-1}}$. The swell pattern was generally composed of multiple components with different directions, but the north-easterly component, which was roughly aligned with the wind, was dominant. The BASE experiment was characterized by strongly varying conditions in terms of wave age, atmospheric stability, wind speed and wind direction. During about 25% of the time unstable conditions with swell prevailed, and included about 185 30-min 'runs', with wind speed in the range 1.5–6 $\mathrm{m\,s^{-1}}$ and a typical significant swell wave height of only 0.3 m.

In a previous study for conditions with swell during the BASE experiment (Smedman et al. 2009; Högström et al. 2009), it was found that the wind profile differs considerably from the shape expected from Monin–Obukhov similarity. Thus, in light winds ($U_{10} = 1.5\,\mathrm{m\,s^{-1}}$), and high wave-age ($c_p/U_{10} = 4.5$) conditions, a wind maximum is found at around 7–8 m above the water surface, with virtually constant wind speed above. For wind speeds in the range 2–6 $\mathrm{m\,s^{-1}}$, wind speed increases rapidly to a height of 7–8 m, being again close to constant with height above that level. The present analysis shows that a very similar wind-profile regime is valid in the RED experiment. In fact, for a case with $U_{10} = 3.2\,\mathrm{m\,s^{-1}}$, a clear wind-speed maximum at $\approx$7 m is observed. Also, for the wind-speed range $3\,\mathrm{m\,s^{-1}} < U_{10} < 6\,\mathrm{m\,s^{-1}}$, wind profiles have a very similar shape to those observed in the BASE experiment, with a rapid increase of wind speed up to $\approx$7 m height and virtually constant wind speed with height above.

It was found that stress and heat flux were close to height constant in the RED experiment, but that Monin–Obukhov theory did not apply. As also found in the BASE experiment, the dimensionless wind gradient ϕ_m in the RED experiment increases from unity at the surface to values in the range 2–4 at $\approx$7 m height, being close to zero at larger heights. In the RED experiment, the highest mean 10 m wind speed is about $10\,\mathrm{m\,s^{-1}}$. Even in that case, which has $c_p/U_{10} = 0.95$, ϕ_m behaves in the way described above, i.e. MO theory does not apply. The strong similarity of the results from the RED and BASE experiments indicates that it is reasonable to expect this to be generally valid in swell-dominated situations, at least where the swell is travelling with or perpendicular to the wind (note that counter-swell cases were not studied here). This is important to bear in mind in the interpretation of results from oceanic experiments with wind measurements at only one level, which is very common practice. In particular, the indiscriminate use of the logarithmic wind profile in such cases can result in completely misleading results, and an attempt to 'correct' the wind profile for stability is not likely to improve the result.

All terms in the TKE budget were evaluated from the RED experiment for four periods with reasonably steady-state conditions consisting each of 8–16 successive 30-min 'runs'. They represent mean wind speed of respectively 3.2, 6.1, 8.0 and 9.7 $\mathrm{m\,s^{-1}}$. All four TKE plots were found to be qualitatively similar to three cases with mean wind speed 4.0, 4.5 and 5.5 $\mathrm{m\,s^{-1}}$ respectively in the BASE experiment (Smedman et al. 2009; Högström et al. 2009). In particular, all these studies from the RED and BASE experiments show an appreciable upward momentum transport through pressure transport from the swell waves to the atmosphere, which decreases exponentially with height, together with a downward pressure transport related to shorter waves in the lowest 7 m.

A further feature that agrees well in the RED and BASE experiments is the relation between the locally wind induced wave energy $E2$ and the 10-m wind speed. $E2$ is defined as the energy in the part of the wave energy spectrum for $n > n_0$, where the frequency n_0 is defined by the requirement that the corresponding wave phase speed $c_0 = 1.2U_{10}$, which, for deep water gives $n_0 = 0.83g/(2\pi U_{10})$. For both experiments it is found that $E2 = 10^{-3}U_{10}^4/g^2$

is an excellent fit, in agreement with results from several other oceanic experiments, as noted earlier.

An important feature that is found to be very different in the BASE and RED experiments during swell is the drag coefficient, C_D. Note that a transformation to the 'neutral' drag coefficient, C_{DN}, is meaningless for swell, since MO theory is not applicable. The notable feature found in this study is that C_D is much larger in the RED experiment than in the BASE experiment at any wind speed in the range $2\,\mathrm{m\,s^{-1}} < U_{10} < 6\,\mathrm{m\,s^{-1}}$. Data from the RED experiment agree very well with corresponding data from the TOGA COARE, and reasonably well with data from the SCOPE (data taken from data in Grachev and Fairall 2001). At $U_{10} = 2.5\,\mathrm{m\,s^{-1}}$ the TOGA COARE value for C_D is about four times greater than the corresponding value from the BASE experiment; in the case of SCOPE, the corresponding factor is about three. In the range between 1.5 and $2\,\mathrm{m\,s^{-1}}$, all data go to zero. For even lower wind speeds, Grachev and Fairall (2001) and Grachev et al. (2003) found negative values for C_D, i.e. net upward momentum transfer. Such observations have been reported before, i.e. Makova (1975) and Smedman et al. (1994). These findings are also in agreement with the results from the large-eddy simulation of Sullivan et al. (2008). The mechanism behind the strongly increased C_D values in situations with high swell will be described in a forthcoming paper.

Acknowledgements The RED measurements were funded by ONR under the Grant N00014-11-10447. The dataset was kindly put to the disposal of the Uppsala group by Tihomir Hristov, and we acknowledge the valuable contributions of our late friend and colleague Carl Friehe. WD acknowledges support from the US National Science Foundation, Grant OCE-0220459 for the BASE measurements.

Disclaimer One of the co-authors, Tihomir Hristov, does not fully agree with the conclusions of this paper and makes the following statement. Multiple departures from the Monin–Obukhov similarity theory have been reported from measurements over land (e.g. Panofsky 1974; Wyngaard 1992; Foken 2006). Some common causes are non-stationary atmospheric conditions and/or non-uniformity (e.g. mesoscale pressure gradients). Vertical variations of the kinematic Reynolds stress $\tau(z) = u_*^2(z)$ and the effective friction velocity $u_*(z)$ occur consequently in the surface layer, with $u_*(z)$ allowing to be presented as $u_*(z) = \bar{u}_* + u'_*(z)$. In such conditions the equation for the wind profile $U(z)$ takes the form $(\frac{\kappa z}{u_*(z)})\frac{\partial U}{\partial z} = \varphi_m(z/L)$ or $(\frac{\kappa z}{\bar{u}_*})\frac{\partial U}{\partial z} = \varphi_m(z/L)\left(1 + \frac{u'_*(z)}{\bar{u}_*}\right)$, indicating that non-stationarity and/or non-uniformity are capable of deforming the wind profile from its Monin–Obukhov-predicted shape. From these considerations one of the authors, T.H., suggests that deviations from Monin–Obukhov theory observed over the ocean cannot be ascribed uniquely to the surface waves and that the surface wave influence on the wind profile is too small to be distinguished with certainty from the alternative influences above, commonly present both overland and over the ocean. Instead, studies of the wave-induced fields in the air appear as a reliable and productive approach to quantifying the wave influence on the atmospheric surface layer.

Appendix

Evaluation of Mean Values of Each Term in the TKE Budget for the Data from the RED Experiment

The Appendix in Högström et al. (2009) presents details of the evaluation procedure that will not be repeated here. Instead, the present discussion will focus on aspects that differ in a significant way. The Högström et al. (2009) Appendix also gives a detailed account of an error estimation, which is not repeated here. The important conclusion from this error analysis was that, typically, the resulting error for the pressure transport term T_p, which is derived as a residual, is about ±50% of the mean values.

The Mechanical Production Term P

For the height interval 5.1–13.8 m, the finite difference method, Eq. 6 was used, and in order to obtain an approximation of P also for the layer below 5.1 m, the method illustrated in Fig. 11 was applied. There the measured wind-speed values are plotted in a linear–logarithmic representation for the case A (Table 2). Near the surface it is expected that the profile will approach the logarithmic form, so that, for small enough z,

$$\frac{\partial U}{\partial z} = \frac{u_*}{kz}. \tag{13}$$

The dashed curve in Fig. 11 is a second-order fit in $\ln z$ of the wind profile

$$U = A \ln z + B(\ln z)^2 + C. \tag{14}$$

The three constants A, B and C are obtained by the requirements that $U_{5.1} = 3.02\ \mathrm{m\ s^{-1}}$ $(\mathrm{d}U/\mathrm{d}z)_{5.1} = (U_{6.9} - U_{5.1})/(6.9 - 5.1) = 0.13$ and, assuming further that Eq. 13 is valid at $z = 1.0$ m, and $u_* = 0.114\ \mathrm{m\ s^{-1}}$, giving

$$U = 2.25 + 0.29 \ln z + 0.113(\ln z)^2. \tag{15}$$

For the determination of P the derivative of Eq. 15 is required,

$$\frac{\partial U}{\partial z} = \frac{0.29}{z} + \frac{0.226 \ln z}{z}, \tag{16}$$

which is expected to be valid for $0.75\ \mathrm{m} < z < 5.1$ m. At $z = 0.75$ m the curve (15) has an inflexion point and starts to behave erroneously for lower z values, but this layer is within the direct influence of the waves, so it is not meaningful to attempt to determine a wind gradient

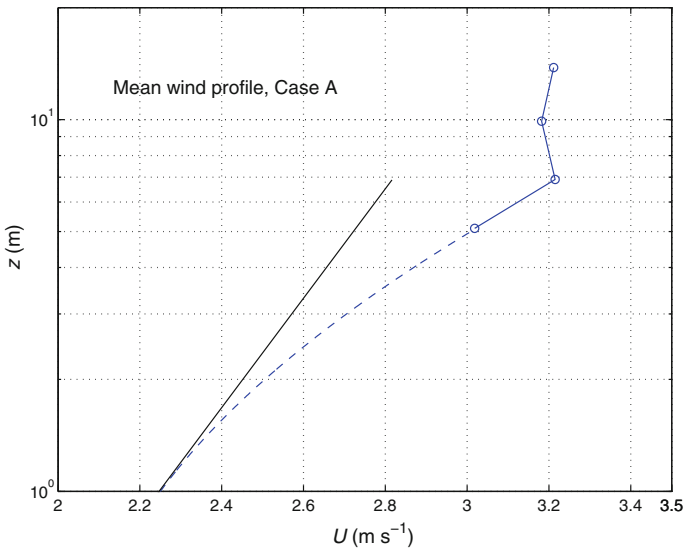

Fig. 11 Mean wind profile for case A in a linear–log representation. Measurements are *open circles* that have been connected by *straight full lines*. The *dashed curve* is a second-order polynomial fit in log z, which fits U and dU/dz at 5.1 m and that has the asymptotic slope $dU/dz = u_*/kz$ for small z (indicated by the *asymptotic line*)

there. At $z = 1.0$ m the wind profile is logarithmic, so that the roughness length z_0 can be evaluated:

$$U = \frac{u_*}{k} \ln(z/z_0). \tag{17}$$

From Eq. (15) we have: $U(1\text{ m}) = 2.25\text{ m s}^{-1}$, so that, with $u_* = 0.114\text{ m s}^{-1}$, we obtain $z_0 = 3 \times 7 \times 10^{-4}$ m, which is a value of reasonable magnitude. Note that case A consists of 16 30-min runs, which gives some reliability to this estimate of z_0.

Dissipation, ε

For the measurement heights, 5.1, 6.9, 9.9 and 13.8 m, dissipation is obtained from the inertial subrange u spectra, which, after invoking Taylor's hypothesis becomes

$$\varepsilon = \frac{2\pi n}{U} \left(\frac{n S_u(n)}{\alpha_1} \right)^{3/2}, \tag{9}$$

where α_1 is a universal constant ≈ 0.50 (cf. Högström 1990 and the text below) and n must be chosen in the region with $-2/3$ slope. The RED spectra are usually well behaved in the inertial subrange, so that application of (9) is straightforward. In neutral conditions, the prediction for ε is

$$\varepsilon = u_*^3 / kz. \tag{18}$$

It is to be expected that Eq. 18 is valid near the surface, and by plotting this relation together with the estimates derived with the inertial subrange method, Eq. 18, an idea of its range of validity may be obtained. Figure 12 shows the result for case A. For this particular case, it appears that Eq. 18 can be used up to $z = 10$ m, since there is reasonable overlap of the inertial subrange estimates at 5.1, 6.9 and 9.9 m with the curve (18). For the other three RED cases evaluated here, Eq. 18 gives a systematic overestimation of ε with about 20% at 5 m, the percentage error increasing further with height. For $z < 5$ m a curve is drawn, which fits the inertial subrange estimate at 10 m and asymptotically approaches Eq. 18 with decreasing height.

Buoyancy Production, B and Turbulent Transport, T_t

The buoyancy production term, B turns out to be relatively small compared to the leading terms and varies only little with height, so an extrapolation down to the surface is straightforward. The turbulent transport term T_t has been evaluated exactly as described in Högström et al. (2009), and it is found to be small compared to the leading terms, so linear extrapolation of the data down to the surface is considered reasonable. The terms B and T_t are both small compared to the leading terms (P, T_p and ε), and they are of opposite sign, making the sum $B + T_\mathrm{t}$ close to zero.

The Pressure Transport Term, T_p

The pressure transport term is obtained from the TKE budget equation as the residual

$$T_\mathrm{p} = -P - B - T_\mathrm{t} - \varepsilon, \tag{19}$$

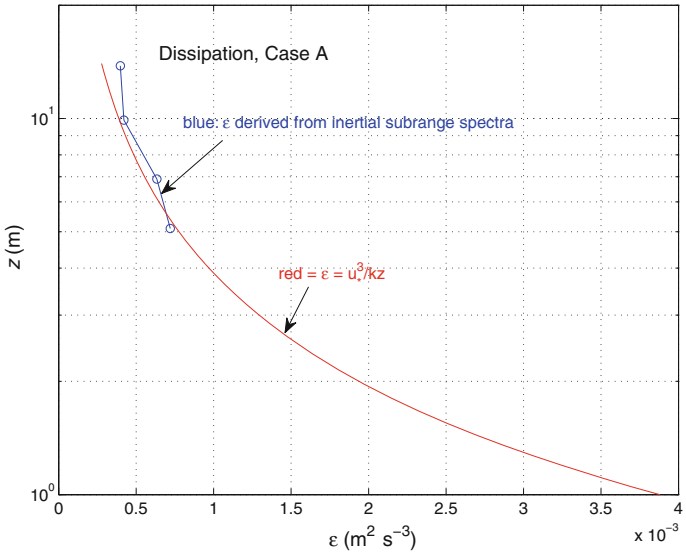

Fig. 12 Dissipation ε, for case A. *Open circles* are estimates derived from inertial sub-range spectra. The *red curve* is the neutral prediction, $\varepsilon = u_*^3/kz$

where P, B, T_t and ε are obtained from the measurements or, for $z < 5$ m, from the expressions outlined above. The values obtained with (19) have been connected with a full line (in magenta), denoted $(T_p)_{tot}$ in the TKE plots, Fig. 10a–e. Above 7 m, all T_p curves become negative, decreasing significantly in magnitude with height. As in Högström et al. (2009), it is assumed that this is the upper part of an exponential curve, which extends down to the surface. For each of the four RED cases, the constant A of the following expression was determined from a best fit to the T_p values at 7, 10 and 14 m

$$(T_p)_{exp} = A \exp(-B_o \kappa z), \tag{20}$$

where $B_o = 1.9$ (see Högström et al. 2009) and κ is the wavenumber of the dominant swell.

For each of the four TKE plots, Fig. 10a–e this curve is plotted as a dashed magenta-coloured line denoted $(T_p)_{exp}$. Also shown, as a cyan-coloured curve, but denoted $(T_p)_s$, is the difference $(T_p)_s = (T_p)_{tot} - (T_p)_{exp}$.

References

Anderson K, Brooks B, Caffre P, Clarke A, Cohen L, Crahan K, Davidson K, De Jong A, De Leeuw G, Dion D, Doss-Hammel S, Fredrickson P, Friehe C, Hristov T, Khelif D, Moerman M, Reid JS, Reising S, Smith M, Terrill E, Tsitikidis D (2004) The RED experiment—an assessment of boundary layer effects in a trade winds regime on microwave and infrared propagation over the sea. Bull Am Meteorol Soc 85:1355–1365

Drennan WM, Kahma KK, Donelan MA (1999) On momentum flux and velocity spectra over waves. Boundary-Layer Meteorol 92:489–515

Drennan WM, Graber HC, Hauser D, Quentin C (2003) On the wave age dependence of wind stress over pure wind seas. J Geophys Res 108(C3):8062. doi:10.1029/2000JC000715

Drennan WM, Taylor PK, Yelland MJ (2005) Parameterizing the sea surface roughness. J Phys Oceangr 35:835–848

Edson J (2008) Review of air–sea transfer processes. In: ECMWF workshop on ocean–atmosphere interactions, 10–12 Nov 2008, Reading, pp 7–24
Fairall CW, Bradley EF, Hare JE, Grachev AA, Edson JB (2003) Bulk parameterization of air–sea fluxes: updates and verifications of the COARE algorithm. J Clim 16:571–591
Fairall CW, Barnier B, Berry DI, Bourassa MA, Bradley EF, Clayson CA, de Leeuw G, Drennan WM, Gille ST, Gulev SK, Kent EC, McGillis WR, Quartly GD, Ryabinin V, Smith SR, Weller RA, Yelland MJ, Zhang H-M (2009) Observations to quantify air–sea fluxes and their role in climate variability and predictability. In: Hall J, Harrison DE, Stammer D, (eds) Proceedings of OceanObs'09: sustained ocean observations and information for society, vol 2, 21–25 Sept 2009, Venice, ESA Publication WPP-306. doi:10.5270/OceanObs09.cwp.27
Foken T (2006) 50 years of the Monin–Obukhov similarity theory. Boundary-Layer Meteorol 119:431–447
Graber HC, Terray EA, Donelan MA, Drennan WM, Van Leer J, Peters DB (2000) ASIS—a new air–sea interaction spar buoy: design and performance at sea. J Atmos Ocean Technol 17:708–720
Grachev AA, Fairall CW (2001) Upward momentum transfer in the marine boundary layer. J Phys Oceangr 31:1698–1711
Grachev AA, Fairall CW, Hare JE, Edson JB, Miller SD (2003) Wind stress vector over ocean waves. J Phys Oceangr 33:2408–2429
Hanley KE, Belcher SE (2008) Wave-driven wind jets in the marine atmospheric boundary layer. J Atmos Sci 65:2646–2660
Holthuijsen LH (2007) Waves in oceanic and coastal waters. Cambridge University Press, Cambridge, UK, 387 pp
Högström U (1990) Analysis of turbulence structure in the surface layer with a modified similarity formulation for near neutral conditions. J Atmos Sci 47:1949–1972
Högström U (1996) Review of some basic characteristics of the ASL. Boundary-Layer Meteorol 78:215–246
Högström U, Sahlée E, Drennan WM, Kahma KK, Smedman A, Johansson C, Pettersson H, Rutgersson A, Tuomi L, Zhang F, Johansson M (2008) Momentum fluxes and wind gradients in the marine boundary layer—a multi-platform study. Boreal Environ Res 13:475–502
Högström U, Smedman A, Sahlée E, Drennan WM, Kahma KK, Pettersson H, Zhang F (2009) The atmospheric boundary layer during swell: a field study and interpretation of the turbulent kinetic energy budget for high wave ages. J Atmos Sci 66:2764–2779
Kolmogoroff AN (1941) Local structure of turbulence in an incompressible fluid at very high Reynolds numbers. Dokl Akad Nauk SSSR 30:299–303
Makova VI (1975) Features of the dynamics of turbulence in the marine atmospheric surface layer at various stages in the development of waves. Atmos Ocean Phys 11:177–182
Panofsky HA (1974) The atmospheric boundary layer below 150 meters. Ann Rev Fluid Mech 6:147–177
Pettersson H, Graber HC, Hauser D, Quentin C, Kahma KK, Drennan WM, Donelan MM (2003) Directional wave measurements from three wave sensors during the FETCH experiment. J Geophys Res 108(C3):806. doi:10.1029/2001JC001164
Pierson WJ, Moskowitz L (1964) A proposed spectral form for fully developed wind seas based on the similarity theory of S.A. Kitaigorodskii. J Geophys Res 69(24):5181–5190
Sahlée E, Drennan WM, Potter H, Rebozo MA (2012) Waves and air–sea fluxes from a drifting ASIS buoy during the Southern Ocean Gas Exchange experiment. J Geophys Res 117:C08003. doi:10.1029/2012JC008032
Semedo A, Saetra Ø, Rutgersson A, Kahma KK, Pettersson H (2009) Wave-induced wind in the marine boundary layer. J Atmos Sci 66:2256–2271
Semedo A, Sušelj K, Rutgersson A, Sterl A (2011) A global view on wind sea and swell climate and variability from ERA-40. J Clim 24:1461–1479
Smedman A, Tjernström M, Högström U (1994) The near-neutral marine atmospheric boundary layer with no shearing stress: a case study. J Atmos Sci 51:3399–3411
Smedman A, Högström U, Bergström H (1997) The turbulence regime of a very stable marine airflow with quasi-frictional decoupling. J Geophys Res 102(C9):21049–21059
Smedman A, Högström U, Bergström H, Rutgersson A, Kahma KK, Pettersson H (1999) A case study of air–sea interaction during swell conditions. J Geophys Res 104:25833–25851
Smedman A, Guo-Larsén X, Högström U, Kahma KK, Pettersson H (2003) Effect of sea state on the exchange over the sea during neutral conditions. J Geophys Res 108:31–113
Smedman A, Högström U, Sahlée E, Drennan WM, Kahma KK, Pettersson H, Zhang F (2009) Observational study of marine atmospheric boundary layer characteristics during swell. J Atmos Sci 66:2747–2763
Sullivan PP, Edson JB, Hristov T, Mc Williams JC (2008) Large eddy simulations and observations of atmospheric marine boundary layers above non-equilibrium surface waves. J Atmos Sci 65:1225–1245
Wyngaard JC (1992) Atmospheric turbulence. Ann Rev Fluid Mech 24:205–234